Differential cross section measurements of the 6.13 MeV gamma ray from proton-induced reaction of fluorine

Differential Cross Section Measurements of the 6.13 MeV Gamma Ray from Proton-Induced Reaction of Fluorine

M. V. Pham[a,*], L. A. Kesler[b], K. B. Woller[b], Z. S. Hartwig[a]

[a] *77 Massachusetts Ave., Department of Nuclear Science and Engineering, Cambridge, MA*
[b] *167 Albany St., Plasma Science and Fusion Center, Cambridge, MA*

Abstract

Fundamental cross section measurements are essential for particle-induced gamma emission (PIGE) analysis. ^{19}F(p,$\alpha\gamma_{2-0}$)^{16}O can be utilized in PIGE analysis; however, differential cross section measurements for this reaction do not exist due to the difficulty in deconvolving overlapping peaks in the gamma spectrum. Although gamma yield measurements for this reaction exist [1], these can only be used for relative measurements. This work presents the 6.13 MeV gamma production differential cross sections for the ^{19}F(p,$\alpha\gamma_{2-0}$)^{16}O reaction in the incident proton kinetic energy range of 837 to 1517 keV. The yield of the 6.13 MeV gamma was obtained by subtracting the contribution of the 7.12 MeV double escape peak using the experimentally-determined ratio of the escape peaks. The corrected yields were converted to differential cross sections, which are presented here for the first time, as a contribution to the current knowledge and utilization of PIGE techniques.

Keywords: Particle-Induced Gamma Emission (PIGE), Fluorine, Ion Beam Analysis (IBA), Nuclear Cross Section

*Corresponding author
Email addresses: mpham@mit.edu (M. V. Pham), kesler@mit.edu (L. A. Kesler), kbwoller@mit.edu (K. B. Woller), hartwig@mit.edu (Z. S. Hartwig)

1. Introduction

PIGE (particle-induced gamma emission) is a highly sensitive IBA (ion beam analysis) technique used to detect low-Z isotopes in surfaces [2]. This technique is advantageous because it has better depth resolution than many other IBA techniques, in addition to allowing more flexibility in detector placement because of the high penetration of gamma rays. However, this technique is limited by the knowledge of differential cross sections [3].

Differential cross section data has not been previously recorded for the ^{19}F(p,$\alpha\gamma_{2-0}$)^{16}O reaction. Proton-fluorine reactions are widely used in PIGE analysis, but are limited to the ^{19}F(p,p'γ)^{19}F reaction, which produces several low energy (<2 MeV) gamma rays with documented production cross sections [4], or require the use of a calibrated standard. Using these techniques, PIGE is used in the analysis of fluorine in human enamel [5, 6], determination of fluorine concentration in the atmosphere [7], and detection of toxic man-made fluorinated chemicals in consumer products [8] for example.

Fluorine is used as a depth marker in PIGE analysis because it is a relatively rare low-Z element and produces high energy characteristic gamma lines that are above background. Additionally, fluorine is useful in fusion material diagnostics because it is not intrinsic to fusion devices [9, 10, 11]. Implanted depth markers of fluorine in refractory metals have been used in the Experimental Advanced Superconducting Tokamak to quantify erosion of these promising first wall materials. Currently, this technique is used ex situ, but could be implemented in situ. However, since the technique would be used remotely at large distances to and from the targets and detectors, full calibration of such a diagnostic system with standards may be infeasible. Additionally, lower energy gamma rays, such as the 0.110 and 0.197 MeV gammas produced by the ^{19}F(p,p'γ_{1-0})^{19}F and ^{19}F(p,p'γ_{2-0})^{19}F reactions, respectively, would be difficult to isolate from the continuum present in the nuclear environment of a fusion device [4]. Synthetic diagnostics have been used to simulate such in situ ion beam analysis in Alcator C-Mod [12], but detailed cross sections of reactions of interest are necessary to

be incorporated in such simulations.

Without differential cross section data for the ^{19}F(p,$\alpha\gamma_{2-0}$)^{16}O reaction, PIGE with high energy gamma rays cannot be performed without the use of a calibration standard, and this reaction cannot easily be incorporated into simulations. Although yield measurements for this reaction are available from Dababneh et al. [1] and Dieumegard et al. [13], yield measurements cannot be directly applied to situations that have different background spectra, detector geometries, experimental setups, and high energy continua from the reference data. This work presents the differential cross section values for the production of the 6.13 MeV gamma ray from the ^{19}F(p,$\alpha\gamma_{2-0}$)^{16}O reaction in the incident proton energy range of 837 to 1517 keV, which encompasses the three largest proton energy resonances in the reaction, enabling its use in varying situations and experimental setups.

2. Background

2.1. Ion Beam Analysis Techniques

PIGE is an IBA technique in which prompt gamma rays are detected from nuclear reactions induced by accelerated ions. Gamma yields from a known reaction can be measured when a sample is bombarded with a beam of ions at a fixed energy. PIGE can be used for depth profiling [14] and also can be used when the chemical composition of the sample is known to detect low-Z isotopes in a surface [2],[3].

PIGE is favorable over other IBA techniques for in situ depth profiling for several reasons. It generally has better energy resolution due to strong, narrow resonances in gamma yield which are useful to PIGE because they occur at discrete energies. This technique is also possible in situ because gamma rays are more penetrating than charged particles as they do not experience Coulombic interactions. However, gamma rays do not provide direct information about the depth so gamma yields are typically compared to a proper standard. Because

of this, the use of PIGE is limited by the knowledge of physical properties such as stopping power and differential cross section values [3].

2.2. Protons on Fluorine Reaction

The ^{19}F(p,$\alpha\gamma$)^{16}O reaction is an inelastic nuclear reaction that results in the emission of an alpha particle and an ^{16}O nucleus in an excited state. This reaction includes three of five exit channels of the ^{19}F(p,α)^{16}O* reaction [1]. Of particular interest in this work is the second channel, or the ^{19}F(p,$\alpha\gamma_{2-0}$)^{16}O reaction, which produces a 6.13 MeV gamma ray when the excited oxygen nucleus returns to its ground state.

The energies of the characteristic gamma rays and relative dominance of the characteristic gamma full energy peaks are given in Table 1 [2]. The yield corresponding to each gamma line (γ_1 =6.13 MeV, γ_2 =6.92 MeV, and γ_3 =7.12 MeV) has a different intensity relative to the total yield of ^{19}F(p,$\alpha\gamma$)^{16}O at varying proton energies. For example, at a proton energy of 936 keV, the relative intensity of the 6.13 MeV gamma is 76% while the relative intensities of the 6.92 MeV and 7.12 MeV characteristic gamma rays are 3% and 21% respectively. The relative intensity of the 6.13 MeV characteristic gamma is the highest for all resonances of interest.

2.3. Gamma Yield and Differential Cross Section

Differential cross section can be calculated using the following relation:

$$\frac{d\sigma}{d\Omega} = \frac{Y\,cos(\alpha)}{N\,t\,\epsilon\,\tau\,\Omega}\frac{q_p}{Q} \tag{1}$$

where $\frac{d\sigma}{d\Omega}$ is the differential cross section in $[\frac{cm^2}{sr}]$, Y is the gamma yield, Q is the collected charge in $[C]$, q_p is the charge of the accelerated particle in $[C]$, N is the volumetric density of of the target isotope in $[cm^{-3}]$, ϵ is the intrinsic efficiency of the detector, τ is the transmission of the gamma rays through the material between the source and the detector, Ω is the solid angle in $[sr]$, t is

Table 1: Gamma Energy of ^{19}F(p,$\alpha\gamma$)^{16}O and relative intensities from Barbour et al. [2]

	Relative Intensities (Percent)		
Gamma Energy (MeV)	γ_1 =6.13 MeV	γ_2 =6.92 MeV	γ_3 =7.12 MeV
Proton Energy (keV)			
668	81	0.3	19
872.1	68	24	8
902	>90	<5	<5
936	76	3	21
1283	74	8	18
1348	55	14	31
1371	87	8	5

the thickness of the target $[cm]$, and α is the angle between the incident beam and the normal to the target surface. In this equation, $\frac{t}{cos(\alpha)}$ is the path length of the accelerated particle beam through the target.

In an experimental setup in which geometry and the chemical composition of the target is known, the gamma yield can be measured and the differential cross section can be calculated using Eq. (1). The efficiency and transmission can be determined for a given experimental setup as a function of gamma energy.

2.4. Challenges in Measuring Cross sections for $^{19}F(p,\alpha\gamma_{2-0})^{16}O$

Measuring differential cross section data for ^{19}F(p,$\alpha\gamma_{2-0}$)^{16}O is difficult due to the close proximity of the gamma rays emitted in the other alpha channels and their corresponding single and double escape peaks. Full energy, single escape, and double escape energies are given for the ^{19}F(p,$\alpha\gamma_{2-0}$)^{16}O reaction in Table 2 [15].

Table 2 shows the gamma rays emitted from the ^{19}F(p,$\alpha\gamma$)^{16}O reaction. All three gamma rays are high energy (>6.13 MeV) and produced within a relatively narrow energy range (∼0.99 MeV), which presents detection and spectroscopy challenges. The high energy of the characteristic gamma rays is advantageous in spectroscopy and diagnostic techniques because there are no natural background

Table 2: Gamma Energies Resulting from Excited States of Oxygen in $^{19}F(p,\alpha\gamma)^{16}O$

Peak	Full Energy Peak [MeV]	Single Escape [MeV]	Double Escape [MeV]
γ_1	6.13	5.62	5.11
γ_2	6.92	6.41	5.90
γ_3	7.12	6.61	6.10

peaks in this energy range. However, it is necessary to use a detector with sufficient enough resolution at high energy to resolve each full energy peak and its escape peaks. Additionally, because detector efficiency is typically low at the high energy range of the characteristic gamma rays, the detector must also have sufficient efficiency to collect data on realistic timescales. A $LaBr_3$ scintillation detector is suitable to collect gamma yield data for this reaction due to its adequate efficiency and high resolution that allowed for the peaks of interest to be well resolved from each other.

3. Methods and Materials

3.1. Experimental Equipment

These measurements were performed at the Cambridge Laboratory of Accelerator Studies of Surfaces (CLASS), with a General IONex 1.7 MV Tandetron tandem ion accelerator equipped with a General IONex Model 860 Negative Sputter Ion Source with a solid TiH cathode used to produce proton beams [16]. Beam energy was calibrated using a NaI detector to locate the accelerator terminal set point corresponding to the proton energy resonance in the $^{19}F(p,\alpha\gamma_{2-0})^{16}O$ reaction at 1371 keV incident proton energy.

A $LaBr_3$ detector was chosen to take yield measurements due to its high resolution and moderately high count rate. The $LaBr_3$ detector is a Canberra "LABR-1.5X1.5" model with a cylindrical crystal from Saint-Gobain. The crystal is 1.5 inches in diameter and 1.5 inches in thickness. Waveforms were digitized using a CAEN DT5790M Desktop Digitizer. Current collected on the target was measured using a RBD 9103 USB Autoranging picoammeter and the

provided software. To ensure accurate current collection measurement, electron suppression voltage of -500 V was used on a grid surrounding the target with a hole to allow the incident beam through.

3.2. Experimental Setup

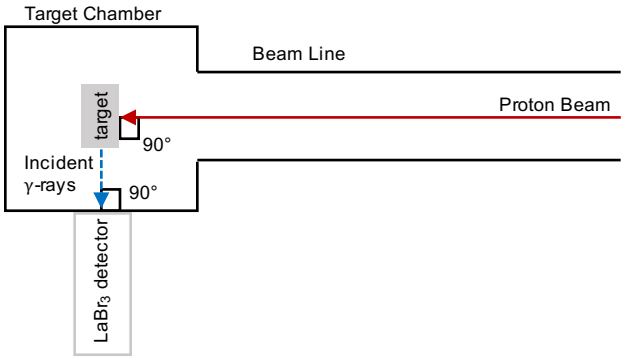

Figure 1: The experimental setup of detector, target, and beam is shown, not to scale. A proton beam was at an incident angle of 90° with respect to the target. The target was a thin film of LiF on the surface of a 3 mm thick molybdenum target.

A proton beam collimated to 3 mm in diameter was focused on a LiF thin film on a molybdenum disc at an incident angle of $\alpha = 0°$ with respect to the normal to the surface in an high vacuum chamber. The vacuum chamber was at a pressure of approximately 10^{-6} torr. The $LaBr_3$ scintillation detector was placed at an angle of 90° with respect to the incident proton beam path flush against a quartz viewport of the chamber. This angle was chosen to maximize gamma rays incident on the detection surface in the experiment setup described. Due to the geometry of the chamber, the detector was placed 20.59 cm away from the target. The beam spot was visualized through this viewport on a scintillating target mounted with the LiF thin film target.

The areal density of fluorine in the LiF thin film was measured with the $^{19}F(\alpha, p)^{22}Ne$ reaction [17] at an incident alpha energy of 2.74 MeV. This reaction was cross-calibrated with a thin CaF_2 coating on paralyene in which backscattered alpha particles and protons from the nuclear reaction were an-

alyzed simultaneously, linking proton yield to fluorine areal density using the calculated backscatter cross section from SigmaCalc [18] within the SimNRA software [19]. Using this method, the F areal density was found to be $6.20 \pm 1.18 \times 10^{21} \frac{1}{m^2}$.

The experimental setup is shown in Fig. 1. In this experimental setup, gamma yield was measured from proton beam energies of 837 keV to 1517 MeV. This energy range was chosen because it contains several of the resonances of ^{19}F(p,$\alpha\gamma$)^{16}O. Additionally, this range is below neutron production thresholds and can be provided by most tandem proton accelerators, minimizing the need for complicated shielding setup and specialized accelerators and sources.

Experimental data was acquired and analyzed using the ADAQ Framework [20], a particle detector data acquisition and analysis package developed at MIT and built on the powerful ROOT toolkit [21]. The ADAQ framework provides real-time control of all data acquisition hardware, live processing and efficient storage of digitized detector data, and a full suite of offline analysis algorithms to process waveforms, create energy deposition spectra, handle background and continuum subtraction, identify and analyze spectral peaks, and other analysis algorithms.

3.3. Analysis Methods

3.3.1. Spectrum Analysis

The raw gamma yield of the ^{19}F(p,$\alpha\gamma$)^{16}O reaction has been measured previously by integrating spectra from energies of approximately 4.5 to 9 MeV in a study by Dababneh et al. [1]. Integration of entire spectra from 4.5 MeV to 9 MeV captures the overlap of the characteristic peaks at 6.13 MeV, 6.92 MeV, and 7.12 MeV with their escape peaks. However, this method does not account for changes in experimental setup and background. Yield measurements can only be used if the experimental setup is exactly the same as that used for the original yield measurements or for relative measurements. Digitized gamma yield data from Dababneh et al. [1] was used to compare and verify yield measurements in this work.

The differential cross section values for 6.13 MeV gamma production from the ^{19}F(p,$\alpha\gamma_{2-0}$)^{16}O reaction were calculated because this peak is the most easily distinguishable due to its high relative intensity over the entire energy range of interest (see Table 1). To calculate these cross sections, the yield of the 6.13 MeV was isolated from the 7.12 MeV double escape peak yield. Yield spectra resulting from data taken at varying proton energies were analyzed using the ROOT framework [21]. Spectra were dynamically calibrated in the high energy range using the full energy peak, single escape peak, and double escape peak of the 6.13 MeV characteristic gamma line. The peaks that were analyzed are shown in Fig 2. To account for possible calibration shift that may have occurred during data collection, each spectrum was divided in sections of 7 to 15 min, depending on the length of data collection, and separately calibrated using process described in following sections.

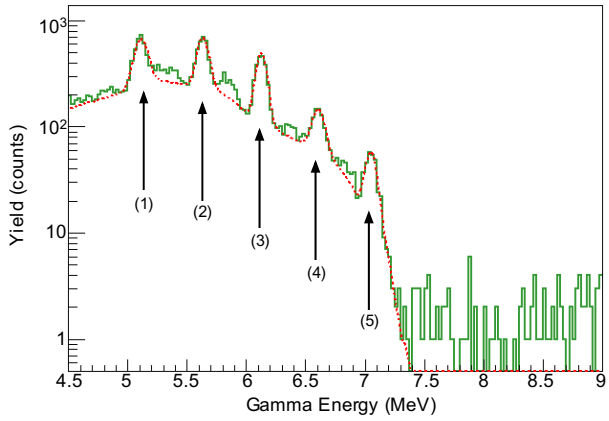

Figure 2: This is a gamma energy spectrum taken for the ^{19}F(p,$\alpha\gamma$)^{16}O reaction at proton energy of 957 $\pm$ 1.2 keV. This spectrum displays the peaks that were integrated to accurately calculate the cross section values of ^{19}F(p,$\alpha\gamma_{2-0}$)^{16}O. (1) 6.13 MeV double escape peak, (2) 6.13 MeV single escape peak, (3) 6.13 MeV full energy peak, (4) 7.12 MeV single escape peak, (5) 7.12 MeV full energy peak. At this proton energy, the 6.92 MeV full energy peak and its escape peaks have too low relative intensity to be seen in this spectrum.

Each peak shown in Fig. 2 was fit with a Gaussian and integrated to obtain the respective yields. To reduce variability in the yield measurements, the

background and continuum were calculated using the SNIP (Sensitive Nonlinear Iterative Peak-clipping) algorithm included in the ADAQ framework and then subtracted from the spectrum [20, 22]. The peaks analyzed in addition to the 6.13 MeV full energy peak were needed to obtain the actual yield of the 6.13 MeV full energy peak. The raw yield of the 6.13 MeV characteristic gamma was corrected by deconvolving the 7.12 MeV double escape peak. The deconvolution of these peaks is described in the following section.

3.3.2. Double Escape Peak to Single Escape Peak Ratio and Deconvolution of Peaks

The double escape of the 7.12 MeV gamma is extremely close in energy to the 6.13 MeV gamma as shown in Table 2, and they are virtually impossible to resolve from each other with any existing detector. Because of this, it is necessary to computationally deconvolve the peaks, which is possible due to the fact that the ratio of the counts in the double escape and the counts in the single escape, R, is independent of the primary energy of the gamma ray and is only a function of detector geometry (which determines the probability of the escape of the 0.511 MeV gammas from the detector) [23, 24]. R is given by the following equation.

$$R = \frac{Quanta\ in\ the\ Double\ Escape\ Peak}{Quanta\ in\ the\ Single\ Escape\ Peak} \tag{2}$$

This ratio can only be determined from escape peaks which are not convolved with any others, such as those of the 6.13 MeV gamma.

For a single detector, R is constant at all energies. R can be exploited to calculate the yield of the 7.12 MeV double escape peak. The peaks needed to determine counts in the 7.12 MeV double escape peak are shown in Fig. 2.

The yields of the peaks shown in Fig. 2 are needed to deconvolve the 6.13 MeV full energy peak and the 7.12 MeV double escape peak.

The constant ratio, R, can be calculated using Eq. 2 and the yields of the 6.13 MeV double and single escape peaks. The actual yield of the 6.13 MeV full energy peak then can be calculated. The actual yield of the 6.13 MeV full

energy peak is given by Eq. 3

$$Y_{actual} = Y_{measured} - R\, Y_{7.12\ MeV\ Single\ Escape} \tag{3}$$

where $Y_{measured}$ is the measured counts in the 6.13 MeV full energy peak, R is the ratio of counts of the double escape peak to counts of the single escape peak, and $Y_{7.12\ MeV\ Single\ Escape}$ is the measured yield in the 7.12 MeV single escape peak.

3.3.3. Single to Double Escape Ratio

The ratio, R, as described in the previous section, was calculated using the single and double escape peaks resulting from the 6.13 MeV gamma from the ^{19}F(p,$\alpha\gamma_{2-0}$)^{16}O reaction. This ratio was also calculated for each spectrum at different proton energies, and the mean was calculated. R was calculated to be 1.03 ± 0.08. Fig. 3 plots the ratio at each proton beam energy in relation to the average ratio value. Nearly all calculated ratio values and their associated error fall within one standard deviation of the average ratio value. Using Eq. (3), the actual yield was measured for each yield measurement at each energy with the average ratio value.

The ratio value was confirmed to be energy independent with an AmBe source with a characteristic gamma energy of 4.4 MeV. The AmBe source was used to confirm the ratio because it produces significantly higher energy gammas than other available check sources resulting in single and double escape peaks that are well defined from the background and continuum with reasonable statistics. The ratio value measured using the AmBe source was found to be 1.01 ± 0.09, which is within error bars of the previously stated ratio value.

4. Results and Discussion

To confirm the locations of the proton energy resonances, gamma yield data was processed in the same technique used by [1] and compared to gamma yield data digitized from the same work. In addition, the 6.13 MeV gamma ray yield

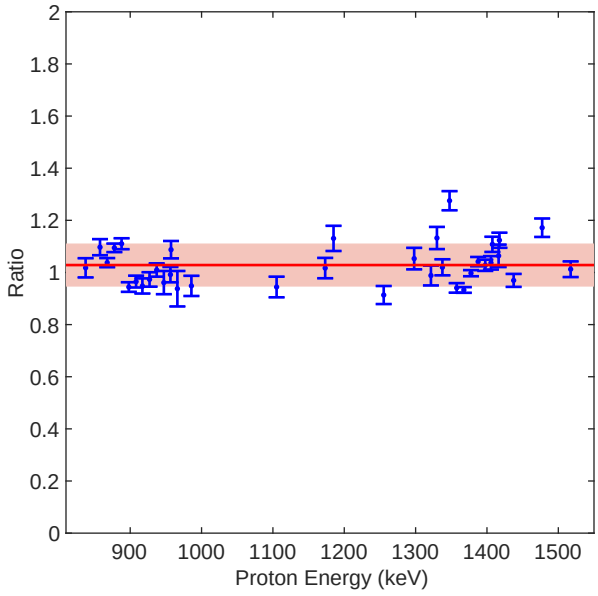

Figure 3: The ratio calculated at each proton beam energy with error bars is plotted. The average value of this ratio is given by the line and the shaded region shows one standard deviation above and below the average.

was compared to digitized data from [1]. The locations of the centroids of the resonances are given in Table 3.

Table 3: Comparison of proton energy resonance centroids in this work to Dababneh et al. [1]. Resonance data from Dababneh et al. [1] was obtained using WebPlotDigitizer. Resonances are labeled 1, 2, and 3 in ascending energy order.

Resonance	Centroid Location [keV]	
	this work	Dababneh et al. [1]
Resonance 1	875 ± 2	870. ± 1
Resonance 2	936 ± 4	930. ± 1
Resonance 3	1371 ± 1	1366 ± 1

As shown in Table 3, the proton resonance energy in this work and from yield data in Dababneh et al. [1] are within 1 percent of each other. This suggests

that gamma yield measured in this work follows previous measurements.

Differential cross section was calculated using Eq. 1. A plot of the differential cross section values vs. proton energy is shown in Fig. 4. The values plotted in Fig. 4 are tabulated in Table 4.

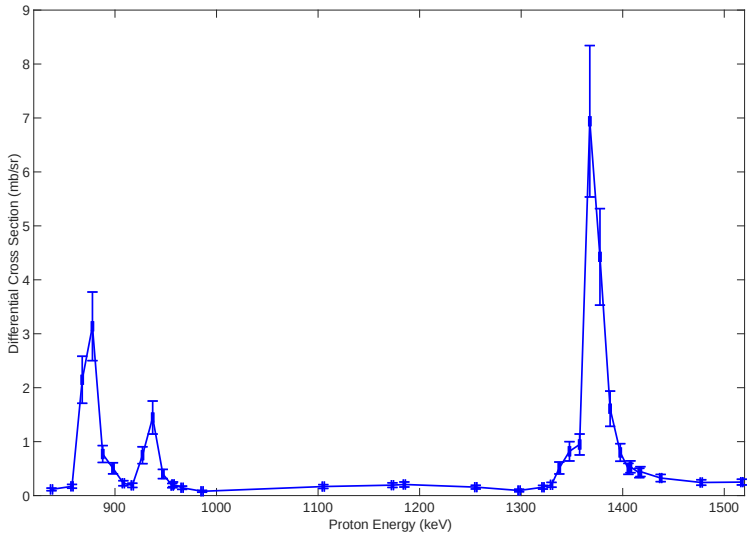

Figure 4: The 6.13 MeV Gamma Production Differential Cross Section Values of from Proton Energy of 837 keV to 1517 keV at 90° angle beam-to-target.

250

Table 4: The 6.13 MeV Gamma Production Differential Cross Section Values for ^{19}F(p,$\alpha\gamma_{2-0}$)^{16}O at 90° angle beam-to-target and their statistical error (1σ)

Proton Energy [keV]	**Differential Cross Section [mb/sr]**
837 ± 1.1	0.11 ± 0.02
858 ± 1.1	0.17 ± 0.04
868 ± 1.1	2.15 ± 0.44
878 ± 1.1	3.14 ± 0.64
888 ± 1.1	0.77 ± 0.16
898 ± 1.1	0.51 ± 0.10

908 ± 1.1	0.23 ± 0.05
917 ± 1.2	0.19 ± 0.04
927 ± 1.2	0.75 ± 0.16
937 ± 1.2	1.45 ± 0.31
947 ± 1.2	0.40 ± 0.09
956 ± 1.3	0.19 ± 0.04
957 ± 1.2	0.21 ± 0.04
966 ± 1.3	0.15 ± 0.03
986 ± 1.3	0.08 ± 0.02
1105 ± 1.2	0.17 ± 0.04
1173 ± 1.2	0.19 ± 0.04
1185 ± 1.2	0.21 ± 0.05
1255 ± 1.2	0.16 ± 0.03
1298 ± 1.2	0.09 ± 0.02
1321 ± 1.1	0.16 ± 0.03
1330 ± 1.2	0.20 ± 0.04
1338 ± 1.1	0.51 ± 0.11
1348 ± 1.2	0.82 ± 0.18
1358 ± 1.2	0.95 ± 0.19
1368 ± 1.2	6.94 ± 1.40
1378 ± 1.2	4.43 ± 0.89
1388 ± 1.2	1.61 ± 0.33
1398 ± 1.2	0.80 ± 0.16
1406 ± 1.1	0.50 ± 0.10
1408 ± 1.2	0.53 ± 0.11
1416 ± 1.2	0.42 ± 0.09
1417 ± 1.1	0.44 ± 0.09
1437 ± 1.2	0.33 ± 0.07
1477 ± 1.2	0.24 ± 0.05
1517 ± 1.2	0.25 ± 0.05

Error in these cross section values result from errors in measurements needed to calculate the cross section. Experimental conditions measured in this setup are given in Table 6. Uncertainty includes statistical error, sample preparation and experimental set up, and data collection methods. These errors are discussed in the following section and presented in Table 7.

Efficiency and transmission curves are found by fitting a function to experimentally collected data points. The calibrated sources used are shown in Table 5. An efficiency curve was created from the four data points using a log fit. This fit was chosen because efficiency can be empirically approximated by a power law [25].

Table 5: Calibrated sources used to calculate efficiency and transmission.

Calibrated Source	Gamma Energy [keV]
Cs-137	662
Mn-54	834.8
Co-60	1173
Co-60	1332

Error in charge collection result from errors in the collection method. With the experimental equipment used to measure charge, errors in charge collection may result from false collection by the software or equipment. Uncertainty measurements of charge collection equipment were provided by the manufacturer.

The accuracy of placement of experimental equipment may result in slight changes of solid angle and incident beam angle causing uncertainty between measurements.

Values of sample number density and sample thickness are determined by sample preparation. Error in these values may be due to error in sample preparation, including irregularities in deposition; contamination; and degradation of the sample over time. Uncertainty due to improper handling is minimized by careful sample handling and collecting yield data in a relatively short time period. The areal density of fluorine in the LiF film was measured using NRA.

This value was found to be $6.20 \pm 1.18 \times 10^{21} \frac{1}{m^2}$.

The charge of the accelerated particle is known from the nuclear reaction and can be found in databases. The error associated in this value is well known and small compared to experimental error.

Another source of error in the cross section measurements may result from possible calibration shift to the detector electronics warming. Calibration shift was accounted for and mitigated by a dynamic calibration method described in Section 3.3.1.

Error in the analysis method and yield measurement greatly contribute to the overall uncertainty due to low count rates and varying relative peak intensities at certain proton energies. Because 6.13 MeV full energy peak is deconvolved with the 7.12 MeV double escape peak to determine the actual yield, error in the yield is affected by the error in the apparent yield of the 6.13 MeV full energy peak, yield of the 7.12 MeV double escape peak, and the ratio of the double escape to single escape peak. Additionally, low count rates lead to longer collection times which may result in greater calibration shift. All contributing error results from statistical error and error in fit and integration methods.

Additional sources of uncertainty may result from uncertainty in the proton beam energy and the calibration of the beam energy. As reported in Table 4, the proton beam energy has an associated error. Although the beam energy was calibrated daily, the additional calibration adds uncertainty to the measurements. If an accelerator with well-known beam energy were used, this additional error could be eliminated. This issue is concerning for proton beam energies near or on resonance due to large differences in count rate. However, because collection times at these energies are generally much shorter, the beam energy is less likely to shift in a short period of time.

5. Conclusion

This work presents differential cross section values for the proton-induced gamma production reaction $^{19}\mathrm{F}(\mathrm{p},\alpha\gamma_{2-0})^{16}\mathrm{O}$. Although gamma yield measure-

Table 6: Experimental conditions

Parameter	Measured Value
Efficiency at 6.13 MeV	0.0161 ± 6%
Transmission at 6.13 MeV	0.954 ± 1%
Detector distance to target	20.59 ± 0.3 cm
Detector solid angle	26.9 ± 0.8 msr

Table 7: Relative errors and uncertainty budget

Parameter	Value	Error	Method of Error Propagation
6.13 MeV Gamma Yield (Y)	437.2 – 8379.4	± 1 – 14 %	Measured
Beam angle (α)	0°	± 5°	Estimated
Collected charge (Q)	0.578 – 5.55 mA	± 0.4% + 200 pA	Manufacturer's estimate
LiF target area density ($N \cdot t$)	6.20×10^{21} $\frac{1}{m^2}$	± 19%	Measured
Efficiency at 6.13 MeV (ϵ)	0.0161	± 6%	Extrapolated from measurement
Transmission at 6.13 MeV (τ)	0.954	± 1%	Extrapolated from measurement
Detector solid angle (Ω)	26.9 msr	± 3%	Estimated
Cumulative error	–	20.2 – 24.7%	–

ments were taken in the prior studies, yield measurements alone can only be used to make relative measurements. Differential cross section values can be used in situations of varying geometry, detector, background, and experimental setup. Differential cross section values can be used in a variety of applications, possibly enabling measurements in fusion materials diagnostics [9, 10, 11], analysis of human enamel [5, 6], and detection of fluorine in consumer products [8] and the atmosphere [7]. It is hoped that while these cross section values have high error values, the techniques and data presented here will allow future researchers to produce data with lower error. Knowledge of differential cross section values is fundamental to the use of IBA techniques such as nuclear reaction analysis (NRA) and PIGE analysis. In addition to expanding databases of differential cross sections, these differential cross section values will contribute

to development of diagnostic techniques that utilize NRA and PIGE.

Acknowledgements

This work was supported by U.S. Department of Energy Grant DE- FG02-94ER54235; and the MIT Undergraduate Research Opportunities Program.

References

[1] S. O. F. Dababneh, K. Toukan, I. Khubeis, Excitation function of the nuclear reaction ^{19}F(p,$\alpha\gamma$)^{16}O in the proton energy range 0.3-3.0 MeV, Nuclear Inst. and Methods in Physics Research, B 83 (3) (1993) 319–324. doi:10.1016/0168-583X(93)95849-Z.

[2] J. C. Barbour, C. J. Maggiore, J. W. Mayer, Handbook of Modern Ion Beam Materials Analysis, 1st Edition, Materials Research Society, Pittsburgh, 1995.

[3] M. Kokkoris, Nuclear Reaction Analysis (NRA) and Particle-Induced Gamma-Ray Emission (PIGE), American Cancer Society, 2012, pp. 1–18. doi:https://doi.org/10.1002/0471266965.com093.pub2.

[4] Development of a Reference Database for Particle Induced Gamma Ray Emission (PIGE) Spectroscopy, no. 1822 in TECDOC Series, INTERNATIONAL ATOMIC ENERGY AGENCY, Vienna, 2017.
URL https://www.iaea.org/publications/12235/development-of-a-reference-database-for-particle-induced-gamma-ray-emission-pige-spectr

[5] H. Komatsu, H. Yamamoto, Y. Matsuda, T. Kijimura, M. Kinugawa, K. Okuyama, M. Nomachi, K. Yasuda, T. Satoh, S. Oikawa, Fluorine analysis of human enamel around fluoride-containing materials under different pH-cycling by -PIGE/PIXE system, in: Nuclear Instruments and Methods in Physics Research, Section B: Beam Interactions with Materials and Atoms, Vol. 269, 2011, pp. 2274–2277.
URL http://dx.doi.org/10.1016/j.nimb.2011.02.042

[6] K. Okuyama, H. Komatsu, H. Yamamoto, P. N. R. Pereira, A. K. Bedran-Russo, M. Nomachi, T. Sato, H. Sano, Fluorine analysis of human dentin surrounding resin composite after fluoride application by -PIGE/PIXE analysis, in: Nuclear Instruments and Methods in Physics Research, Section B: Beam Interactions with Materials and Atoms, Vol. 269, 2011, pp. 2269–2273.
URL http://dx.doi.org/10.1016/j.nimb.2011.02.063

[7] F. Calastrini, P. Del Carmine, F. Lucarelli, P. A. Mandò, P. Prati, A. Zucchiatti, External-beam PIGE for fluorine determination in atmospheric aerosol, Nuclear Instruments and Methods in Physics Research, Section B: Beam Interactions with Materials and Atoms 136-138 (1998) 975–980.
URL http://dx.doi.org/10.1016/S0168-583X(97)00750-7

[8] E. E. Ritter, M. E. Dickinson, J. P. Harron, D. M. Lunderberg, P. A. DeYoung, A. E. Robel, J. A. Field, G. F. Peaslee, PIGE as a screening tool for Per- and polyfluorinated substances in papers and textiles, Nuclear Instruments and Methods in Physics Research, Section B: Beam Interactions with Materials and Atoms 407 (2017) 47–54.
URL http://dx.doi.org/10.1016/j.nimb.2017.05.052

[9] Z. Hartwig, H. Barnard, B. Sorbom, R. Lanza, B. Lipschultz, P. Stahle, D. Whyte, Fuel retention measurements in Alcator C-Mod using Accelerator-based In-situ Materials Surveillance, Journal of Nuclear Materials 463 (0022-3115) (2015) 73–77. doi:10.1016/j.jnucmat.2014.09.056.

[10] L. Kesler, B. Sorbom, Z. Hartwig, H. Barnard, G. Wright, D. Whyte, Initial results of tests of depth markers as a surface diagnostic for fusion devices, Nuclear Materials and Energy 12 (2017) 1277–1281, proceedings of the 22nd International Conference on Plasma Surface Interactions 2016, 22nd PSI. doi:https://doi.org/10.1016/j.nme.2016.11.013.

[11] L. Kesler, Development and testing of an in situ method of ion beam analysis for measuring high-Z erosion inside a tokamak using an AIMS diagnostic, Ph.D. thesis, Massachusetts Institute of Technology (2018).

[12] Z. S. Hartwig, D. G. Whyte, Simulated plasma facing component measurements for an in situ surface diagnostic on Alcator C-Mod, in: Review of Scientific Instruments, Vol. 81, 2010.
URL http://dx.doi.org/10.1063/1.3478634

[13] D. Dieumegard, B. Maurel, G. Amsel, Microanalysis of Flourine by nuclear reactions: I. ^{19}F(p, α_0)^{16}O and ^{19}F(p, $\alpha\gamma$)^{16}O reactions, Nuclear Instruments and Methods 168 (1) (1980) 93–103. doi:10.1016/0029-554X(80)91237-9.
URL http://www.sciencedirect.com/science/article/pii/0029554X80912379

[14] J. Räisänen, J. P. Hirovenen, R. Lappalainen, Particle-Induced Gamma Emission: PIGE, 2nd Edition, Materials Research Society, Warrendale, Pennsylvania, 2009.

[15] G. F. Knoll, Radiation Detection and Measurement, 4th Edition, John Wiley & Sons, Inc., Hoboken, NJ, 2010.

[16] G. M. Wright, H. S. Barnard, Z. S. Hartwig, P. W. Stahle, R. M. Sullivan, K. B. Woller, D. G. Whyte, Plasma-Surface Interaction Research At The Cambridge Laboratory Of Accelerator Studies Of Surfaces, AIP Conference Proceedings 1336 (1) (2011) 626–630. doi:10.1063/1.3586178.
URL https://aip.scitation.org/doi/abs/10.1063/1.3586178

[17] J. Cseh, E. Koltay, Z. Máté, E. Somorjai, L. Zolnai, Levels in ^{23}Na excited by the ^{19}F(α, α)^{19}F, ^{19}F(α, γ)^{23}Na and ^{19}F(α, p)^{22}Ne reactions, Nuclear Physics A 413 (2) (1984) 311 – 322. doi:https://doi.org/10.1016/0375-9474(84)90377-4.
URL http://www.sciencedirect.com/science/article/pii/0375947484903774

[18] A. Gurbich, Sigmacalc recent development and present status of the evaluated cross-sections for IBA, Nuclear Instruments and Methods in Physics Research Section B: Beam Interactions with Materials and Atoms 371 (2016) 27 – 32, the 22nd International Conference on Ion Beam Analysis (IBA 2015). doi:https://doi.org/10.1016/j.nimb.2015.09.035.
URL http://www.sciencedirect.com/science/article/pii/S0168583X15008940

[19] M. Mayer, Improved physics in SIMNRA 7, Nuclear Instruments and Methods in Physics Research Section B: Beam Interactions with Materials and Atoms 332 (2014) 176 – 180, 21st International Conference on Ion Beam Analysis. doi:https://doi.org/10.1016/j.nimb.2014.02.056.
URL http://www.sciencedirect.com/science/article/pii/S0168583X14003139

[20] Z. S. Hartwig, The ADAQ framework: An integrated toolkit for data acquisition and analysis with real and simulated radiation detectors, Nuclear Instruments and Methods in Physics Research, Section A: Accelerators, Spectrometers, Detectors and Associated Equipment 815 (2016) 42–49. doi:10.1016/j.nima.2016.01.017.
URL http://dx.doi.org/10.1016/j.nima.2016.01.017

[21] R. Brun, F. Rademakers, ROOT - An object oriented data analysis framework, Nuclear Instruments and Methods in Physics Research, Section A: Accelerators, Spectrometers, Detectors and Associated Equipment 389 (1-2) (1997) 81–86. doi:10.1016/S0168-9002(97)00048-X.

[22] M. Morháč, J. Kliman, V. Matoušek, Background elimination methods for multidimensional coincidence γ-ray spectra, Nucl. Instr. Meth. Phys. Res. A 401 (97) (1997) 113–132. doi:10.1016/S0168-9002(97)01023-1.

[23] J. Kopecký, W. Ratyński, E. Warming, Curves for the response of a Ge(Li) detector to gamma rays in the energy range up to 11 MeV, Nuclear Instru-

ments and Methods 50 (2) (1967) 333–339. doi:10.1016/0029-554X(67)90061-4.

[24] J. R. Johnson, K. C. Mann, Single And Double Escape Peaks in Ge(Li) Gamma-Ray Spectra, Nuclear Instruments and Methods 112 (3) (1973) 601–602. doi:10.1016/0029-554X(73)90186-9.
URL https://www.sciencedirect.com/science/article/abs/pii/0029554X73901869

[25] D. Reilly, N. Ensslin, H. Smith, S. Kreiner (Eds.), Passive nondestructive assay of nuclear materials (NUREG/CR–5550), Nuclear Regulatory Commission, 1991.
URL https://inis.iaea.org/search/search.aspx?orig_q=RN:23009217